Including land cover change in analysis of greenness trends using all available Landsat 5, 7, and 8 images: A case study from Guangzhou, China (2000–2014)

Zhe Zhu [a,*], Yingchun Fu [b,*], Curtis E. Woodcock [c], Pontus Olofsson [c], James E. Vogelmann [d], Christopher Holden [c], Min Wang [b], Shu Dai [b], Yang Yu [b]

[a] ASRC InuTeq, Contractor to U.S. Geological Survey (USGS) Earth Resources Observation and Science (EROS) Center, 47914 252nd Street, Sioux Falls, SD 57198, USA
[b] School of Geography, South China Normal University, Guangzhou 510631, PR China
[c] Center for Remote Sensing, Department of Earth and Environment, Boston University, 685 Commonwealth Avenue, Boston, MA 02215, USA
[d] U.S. Geological Survey (USGS),Earth Resources Observation and Science (EROS) Center, Sioux Falls, SD 57198, USA

ABSTRACT

Remote sensing has proven a useful way of evaluating long-term trends in vegetation "greenness" through the use of vegetation indices like Normalized Differences Vegetation Index (NDVI) and Enhanced Vegetation Index (EVI). In particular, analyses of greenness trends have been performed for large areas (continents, for example) in an attempt to understand vegetation response to climate. These studies have been most often used coarse resolution sensors like Moderate Resolution Image Spectroradiometer (MODIS) and Advanced Very High Resolution Radiometer (AVHRR). However, trends in greenness are also important at more local scales, particularly in and around cities as vegetation offers a variety of valuable ecosystem services ranging from minimizing air pollution to mitigating urban heat island effects. To explore the ability to monitor greenness trends in and around cities, this paper presents a new way for analyzing greenness trends based on all available Landsat 5, 7, and 8 images and applies it to Guangzhou, China. This method is capable of including the effects of land cover change in the evaluation of greenness trends by separating the effects of abrupt and gradual changes, and providing information on the timing of greenness trends.

An assessment of the consistency of surface reflectance from Landsat 8 with past Landsat sensors indicates biases in the visible bands of Landsat 8, especially the blue band. Landsat 8 NDVI values were found to have a larger bias than the EVI values; therefore, EVI was used in the analysis of greenness trends for Guangzhou. In spite of massive amounts of development in Guangzhou from 2000 to 2014, greenness was found to increase, mostly as a result of gradual change. Comparison of the greening magnitudes estimated from the approach presented here and a Simple Linear Trend (SLT) method indicated large differences for certain time intervals as the SLT method does not include consideration for abrupt land cover changes. Overall, this analysis demonstrates the importance of considering land cover change when analyzing trends in greenness from satellite time series in areas where land cover change is common.

© 2016 Published by Elsevier Inc.

1. Introduction

1.1. Background

One high profile use of satellite observations has been to track trends in the greenness of vegetation through time, primarily as an indicator of ecosystem response to changes in climate. Increased vegetation growth has been observed in various locations, including the Northern Hemisphere (Jong, Verbesselt, Schaepman, & Bruin, 2012; Myneni, Keeling, Tucker, Asrar, & Nemani, 1997; Piao et al., 2015; Zhou et al., 2001), Australia (Donohue, McVICAR, & Roderick, 2009) and the Sahel region in Central Africa (Herrmann, Anyamba, & Tucker, 2005; Olsson, Eklundh, & Ardö, 2005). The opposite trend (commonly referred to as browning) has also been observed in the forests of the Congo (Zhou et al., 2014) and the arid southwestern United States (Breshears et al., 2005) in recent decades.

Another context for monitoring trends in vegetation greenness concerns the effect of human activity on landscapes. Particularly in urban environments, human actions can lead to either increases or decreases in vegetation greenness. For example, conversion of agricultural land or forests to developed land usually results in a decrease in vegetation

* Corresponding authors.
E-mail addresses: zhezhu@usgs.gov (Z. Zhu), fuyc@m.scnu.edu.cn (Y. Fu).

greenness. Conversely, planting of vegetation in urban environments is a common element of urban planning and can lead to increases in greenness.

Vegetation in and around urban environments has been recognized as providing valuable ecosystem services, including the regulating services of climate regulation, water filtration, and air purification. Trees in urban areas can remove harmful air pollutants including sulfur dioxide, nitrogen oxide, carbon monoxide, and air particulate matter. For example, Nowak, Crane, and Stevens (2006) estimated that trees and shrubs in cities in the United States remove approximately 711,000 Mg of air pollutants in one year, a contribution valued at $3.8 billion U.S. dollars. Similarly, Jim and Chen (2008) modeled the effects of forest vegetation in Guangzhou for the year 2000 and found that the urban forest removed approximately 312.03 Mg of air pollutants.

Vegetation can also have significant effects on local climate. For example, an addition of approximately three trees per building in Chicago is estimated to provide savings of about $50 to $90 per building through heating and cooling cost reductions (McPherson et al., 1997). Trees insulate building in the winter by reducing wind speeds and help cool buildings in the summer by increasing shade and evapotranspiration. In addition to contributing many ecosystem services, urban vegetation improves the quality of life for residents. Jim and Chen (2006) found that citizens of Guangzhou, China, valued access to greenspaces highly, with 96% of the people surveyed willing to pay for access to greenspaces and a collective willingness to pay for greenspaces that was six times the city's annual expenditure for development and maintenance of urban greenspaces.

Access to these ecosystem services is especially important in large and rapidly growing urban environments because the process of urbanization frequently degrades or removes these services. Cities in China have been undergoing dramatic expansion and intensification since the country adopted the "reform and openness" policy in 1978 (Anderson & Ge, 2004; Hun & Wong, 1994). The total urban area in 1996 was almost triple the extent in 1949 (Lin & Ho, 2003). The rate of urban expansion in the Pearl River Delta has been especially noteworthy during the past few decades, increasing more than 300% between 1988 and 1996 (Seto et al., 2002). Guangzhou (Canton), the capital of Guangdong Province located at the mouth of the Pearl River, is one of the oldest and largest cities in China. It has been the center of dramatic economic development and urban expansion (Fu, Lu, Zhao, Zeng, & Xia, 2013). Approximately 92 km^2 of water adjacent to the outlet of the Pearl River were reclaimed to islands between 1978 and 1998, most of which have already been developed (Chen, Chen, Liu, Li, & Tan, 2005). Between 1978 and 2013, 40% of farmlands were converted to other uses (Guangzhou Statistics Yearbook, 2014). Meanwhile, forest cover underwent large fluctuations; for example, based on Guangdong forest inventory data, forest cover increased from 31% to 40% between 1993 and 2003 and decreased from 40% to 36% between 2003 and 2013. In 2000, the Guangzhou government proposed a new development strategy for transforming the city into a world-class metropolis by 2010 (Weng & Yang, 2003). With this vast amount of human activity and the new development strategy announced in 2000, the question of whether greenness has declined or increased in Guangzhou merits further investigation.

1.2. Satellite remote sensing of vegetation greenness

Satellite remote sensing provides the opportunity to analyze vegetation condition over large areas. Vegetation Indices (VIs), such as the Normalized Difference Vegetation Index (NDVI) and Enhanced Vegetation Index (EVI), are widely used to analyze trends in vegetation greenness, due to their high correlation with the amount of chlorophyll, vegetation leaf area, and photosynthetic capacity (Carlson & Ripley, 1997; Huete et al., 2002; Myneni, Hall, Sellers, & Marshak, 1995; Olofsson & Eklundh, 2007; Tucker, 1979). Compared to NDVI, EVI is generally more robust to atmospheric and soil background influences, and

saturates less at high Leaf Area Index (LAI) values (Huete et al., 2002). Analysis of trends in vegetation greenness have generally been focused on very large areas, such as entire continents or portions of continents, and the satellite data employed have been relatively coarse in spatial resolution (Jong et al., 2012; Myneni et al., 1997; Olofsson & Eklundh, 2007; Olofsson et al., 2008; Piao et al., 2015; Zhou et al., 2001). For example, the spatial resolution of the NDVI and EVI datasets generated from Moderate Resolution Image Spectroradiometer (MODIS) is either 250 m, 500 m or 1 km (Huete et al., 2002), and the spatial resolution of NDVI datasets produced from Advanced Very High Resolution Radiometer AVHRR is 8 km (Tucker et al., 2005). To better characterize greenness in and around cities, higher spatial resolution is required.

The sensors of Landsats 4, 5, 7, and 8 provide 30-meter resolution and 16-day revisit cycle (Wulder et al., 2008), allowing effective monitoring of many human-induced land cover changes (Huang et al., 2010; Kennedy, Cohen, & Schroeder, 2007; Masek, Lindsay, & Goward, 2000; Seto & Fragkias, 2005; Yuan, Sawaya, Loeffelholz, & Bauer, 2005), as well as characterizing greenness trends at local or regional scales for a variety of environments, including forests (Lehmann, Wallace, Caccetta, Furby, & Zdunic, 2013; Vogelmann, Tolk, & Zhu, 2009; Vogelmann, Xian, Homer, & Tolk, 2012), drylands (Sonnenschein, Kuemmerle, Udelhoven, Stellmes, & Hostert, 2011), and Arctic tundra (Fraser, Olthof, Carrière, Deschamps, & Pouliot, 2012). It is important to note, that the work presented in this paper is focused on urban environments, and as such represents a different context for monitoring greenness trends with Landsat data as human activity is the primary driver of changes in greenness. In particular, land cover change generally causes abrupt changes in vegetation greenness, and in the work presented here we attempt to separate these abrupt changes from more gradual changes in vegetation greenness.

Most studies of vegetation trends using Landsat are based on the Thematic Mapper (TM) sensor on Landsats 4 and 5 and the Enhanced Thematic Mapper Plus (ETM+) sensor on Landsat 7, because these sensors are well calibrated with each other (Barsi et al., 2003; Chander, Markham, & Helder, 2009; Teillet et al., 2001). Although Landsat 5 is no longer in service, and Landsat 7 has been hampered by the failure of the Scan Line Corrector (SLC-off), the successful launch of Landsat 8 has provided continuity of moderate spatial resolution data that can be used for long-term trend analysis (Roy et al., 2014).

The Landsat 8 satellite carries two sensors, the Operational Land Imager (OLI) and the Thermal Infrared Sensor (TIRS) (Irons, Dwyer, & Barsi, 2012). Compared to TM and ETM+, OLI has two new spectral bands: an ultra-blue band (0.43–0.45 μm), and a cirrus band (1.36–1.39 μm) (Table 1). The ultra-blue band is designed primarily for characterizing coastal waters and atmospheric aerosol properties, and the cirrus band is mainly intended to facilitate better detection of thin cirrus clouds (Kovalskyy & Roy, 2015; Zhu, Wang, & Woodcock, 2015). In general, the OLI bands are spectrally narrower than the corresponding ETM+ bands, especially in the near-infrared (NIR) region. TIRS has two thermal bands that are also narrower than the ETM+ thermal bands, and are located at different wavelengths for the purposes of retrieving surface temperature (Rozenstein, Qin, Derimian, & Karnieli, 2014). Considering all these factors, it is important to ensure that data from Landsat 8 are consistent with data from the previous Landsat sensors before they are combined with data from other sensors in trend analysis.

To date, several studies have explored the consistency of data from Landsat 7 and Landsat 8 by comparing clear-sky observations for the same location, but acquired 8 days apart (Flood, 2014; Li, Jiang, & Feng, 2014). These studies have been based on the assumption that there is no phenology or land cover change between acquisitions. It has been reported that the top-of-atmosphere reflectance differences between the two sensors can be as large as 6%, with differences in surface reflectance of about 2% and NDVI differences about 5% (Flood, 2014). Conversely, Li et al. (2014) analyzed the consistency between sensors for a variety of vegetation indices and surface reflectances and

Table 1

Comparison of Landsat 8 Operational Land Imager (OLI) and Thermal Infrared Sensor (TIRS) bands with Landsat 7 Enhanced Thematic Mapper Plus (ETM +) and Landsat 5 Thematic Mapper (TM) bands (the bands in bold letters are the bands used in this study).

Landsat 8 (OLI & TIRS)		Landsat 7 (ETM +)		Landsat 5 (TM)	
Band description	Wavelength (μm)	Band description	Wavelength (μm)	Band description	Wavelength (μm)
Band 1 — Ultra blue	0.43–0.45				
Band 2 — Blue	0.45–0.51	**Band 1 — Blue**	0.45–0.52	**Band 1 — Blue**	0.45–0.52
Band 3 — Green	0.53–0.59	**Band 2 — Green**	0.52–0.60	**Band 2 — Green**	0.52–0.60
Band 4 — Red	0.64–0.67	**Band 3 — Red**	0.63–0.69	**Band 3 — Red**	0.63–0.69
Band 5 — NIR	0.85–0.88	**Band 4 — NIR**	0.77–0.90	**Band 4 — NIR**	0.76–0.90
Band 6 — SWIR1	1.57–1.65	**Band 5 — SWIR1**	1.55–1.75	**Band 5 — SWIR1**	1.55–1.75
Band 7 — SWIR2	2.11–2.29	**Band 7 — SWIR2**	2.09–2.35	**Band 7 — SWIR2**	2.08–2.35
Band 8 — Pan	0.50–0.68	Band 8 — Pan	0.52–0.90		
Band 9 — Cirrus	1.36–1.38				
Band 10 — TIR	10.60–11.19	**Band 61 — TIR**	10.40–12.50 (high gain)	**Band 6 — TIR**	10.40–12.50
Band 11 — TIR	11.50–12.51	Band 62 — TIR	10.40–12.50 (low gain)		

concluded that ETM+ and OLI images are similar enough to be used as complementary data. However, in the analysis of greening trends, a 5% change in NDVI can be significant. Therefore, it is important to quantify the differences between Landsat 8 and prior Landsat sensors before their combined use for trend analysis.

1.3. Methods for analyzing greenness trends

Most studies of greenness trends assume there is little or no land cover change in the study area and are interested in overall trends related to external factors like climate (Bhatt et al., 2013; Fraser et al., 2012; Lehmann et al., 2013; Myneni et al., 1997; Piao et al., 2015; Sonnenschein et al., 2011; Vogelmann et al., 2012). Based on a simple linear regression of the VIs, a slope coefficient can be easily generated, which has typically been used to represent the long-term trend in greenness (referred to here as the Simple Linear Trend (SLT) method). This method may work well for areas that are not undergoing substantial land cover change, but for areas characterized by major land cover change, this approach may provide results that are misleading or incomplete. The effect of land cover change is especially relevant in Guangzhou, as it is one of the fastest growing megacities in the world (Seto et al., 2002). If a place has been disturbed multiple times, the SLT model can produce misleading results. Therefore, for accurate quantification of trends in greenness in megacities such as Guangzhou, we need to distinguish between the abrupt changes caused by land cover change from gradual changes (greening or browning) in places where land cover change has not occurred.

Many algorithms have been developed for detecting land cover change by analyzing time series of satellite data (Hermosilla, Wulder, White, Coops, & Hobart, 2015; Huang et al., 2010; Kennedy et al., 2007; Masek et al., 2008; Seto & Fragkias, 2005; Verbesselt, Hyndman, Newnham, & Culvenor, 2010; Yang & Lo, 2002), but few studies have included land cover change information in analyzing greenness trends. In fact, in most studies there has been an explicit effort to exclude areas of land cover change from analysis of greenness trends as climate rather than the effect of human activity was the primary focus of the studies. However, Jong et al. (2012) separately quantified abrupt and gradual changes globally based on time series of NDVI from AVHRR using the Breaks For Additive Season and Trend (BFAST) procedure (Verbesselt et al., 2010). This innovative work laid a foundation upon which the work presented here is based. However, there are several differences between what we propose and that of Jong et al. (2012). For example, their work was done at coarse spatial resolution (~8km), and thus may not accurately detect human-induced land cover changes like those found in Guangzhou that usually occur at finer spatial scales. Also, since Jong et al. (2012) relied solely on NDVI, it is possible that land cover changes that are more apparent in other spectral dimensions may have been missed. One of the difficulties associated with working at AVHRR scales is that it is hard to identify land cover types, as well

as land cover change. Jong et al. (2012) used the 2009 MODIS land cover product (Friedl et al., 2002; Friedl et al., 2010) to represent land cover from 1982 to 2008. While this may not introduce large errors at the global scale, it could be problematic for local- or regional-scale studies, such as in Guangzhou. In this study, we use the CCDC (Continuous Change Detection and Classification) algorithm (Zhu & Woodcock, 2014a, Zhu, Woodcock, Holden, & Yang, 2015) and all available Landsat data for detecting both abrupt and gradual changes in greenness, as well as for providing land cover information at scales relevant to human activities. Therefore, we have the opportunity to compare the differences in greenness trends depending on whether or not land cover change is taken into account.

Three major questions are considered in this study:

1) Has the greenness of Guangzhou been increasing or decreasing in the period from 2000 to 2014?
2) Can Landsat 8 data be combined with data from prior Landsat sensors for analysis of greenness trends?
3) How does accounting for the influence of land cover change affect monitoring of greenness trends?

2. Study area and data

2.1. Study area

Guangzhou (22°26′–23°56′N, 112°57′–114°03′E) is located on the northern edge of the Pearl River Delta in South China (Fig. 1). It covers an area of 7434 km², with a population of 8.32 million as of 2012 (Guangzhou Statistics Yearbook, 2014). The warm and rainy climate provides favorable conditions for vegetation growth. Guangzhou City is composed of ten urban districts and two country-level cities. The economy of Guangzhou has grown tremendously with the regional Gross Domestic Product increasing from $32 billion in 1990 to $1688 billion in 2014 (Guangzhou Yearbook Compilation Committee, 2010).

2.2. Landsat data

All available Level 1 Terrain (Corrected) (L1T) Landsat 5, 7, and 8 images acquired from 1999 to 2014 with more than 20% clear observations (i.e. pixels with no clouds, cloud shadows or snow) were used for WRS-2 Path 122 and Row 44 . The percentage of clear observations was estimated by Fmask, which is an object-based cloud, cloud shadow, and snow detection algorithm (Zhu, Wang, & Woodcock, 2015; Zhu & Woodcock, 2012). A total of 194 Landsat images were used in the analysis, of which 61 images were from Landsat 5 (acquired from January 26, 2000 to April 27, 2010), 120 images were from Landsat 7 (acquired from October 14, 1999 to June 1, 2014), and 13 images were from Landsat 8 (acquired from July 8, 2013 to September 29, 2014). For each Landsat image, 7 spectral bands were used in this study: three
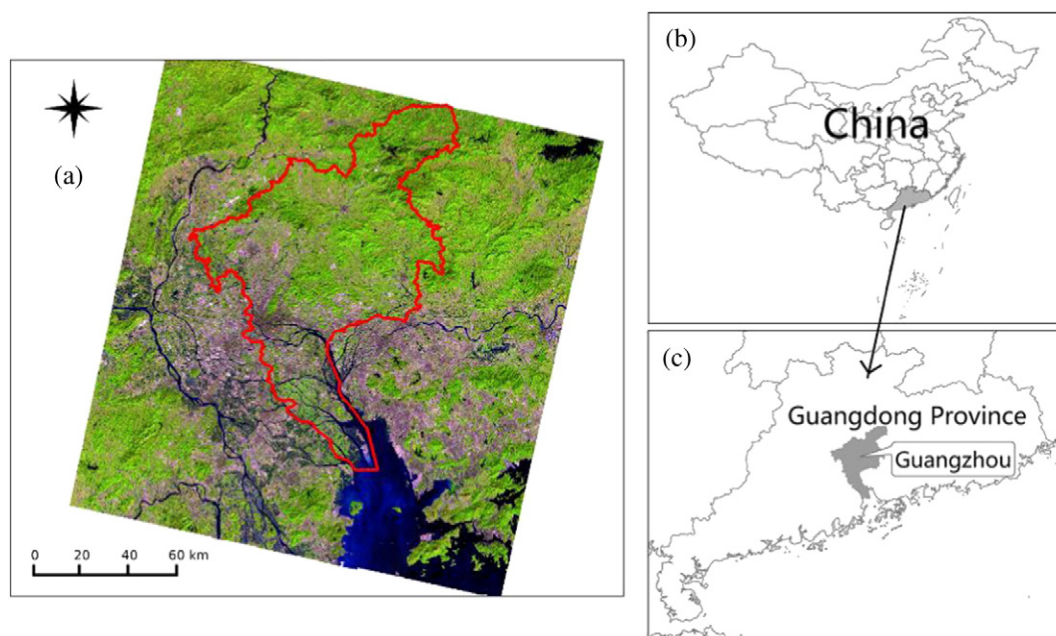
Fig. 1. Study area. The background in Fig. 1a is a shortwave-infrared, near-infrared, and green-visible RGB false-color composite Landsat 8 image acquired on November 29, 2013. The red polygon is the boundary of Guangzhou city.

visible bands (blue, green, and red), one NIR band, two shortwave-infrared bands (SWIR 1 and SWIR 2), and a thermal infrared (TIR) band (indicated by bold letters in Table 1). All 7 spectral bands were used for land cover classification, and 5 spectral bands were applied for change detection. The blue and TIR bands were excluded in the change detection analysis due to their sensitivity to atmospheric contamination (Zhu, Woodcock, Holden, & Yang, 2015). To check the consistency of Landsat 8 data with earlier Landsat data, we assessed surface reflectance of the 6 optical bands and two VIs (NDVI and EVI).

Table 2
14-categories land cover description.

Classes	Number of Pixels	Description
Evergreen Needleleaf Forest (ENF)	241	Forested land > 80% coniferous evergreen canopy cover
Evergreen Broadleaf Forest (EBF)	438	Forested land > 80% broadleaved evergreen canopy cover
Mixed Forest (MF)	188	Mosaic of multiple forest species, with no single canopy greater than 60%
Secondary Forest (SF)	280	Plantation forested land > 80% after forest harvest, with unique species
Croplands (C)	563	Managed plantation of crop followed by harvest paddy and bared soil
Orchard (O)	284	Managed plantation of fruit trees, primarily litchi and banana
Shrubland (S)	175	Woody vegetation cover less than 2 m tall and > 50% shrub species
Grassland (G)	417	Grassland dominated open space with < 10% tree and shrub cover
Wetland (WL)	201	Vegetated lands with a high water table
Water (W)	600	Standing water present >11 months, oceans, lakes, rivers, and water pond
Barren (B)	367	Bare land sparsely vegetated, > 60% soil background
Low Density Residential (LDR)	403	Residential land with equal parts impervious surface & vegetation
High Density Residential (HDR)	376	Residential land minimally vegetated, > 60% impervious surface
Commercial/Industry (CI)	537	Impervious surface and man-made building > 80%

2.3. Training data

Training data were extracted from the 14-category (see Table 2 for class descriptions) Land Use Inventory Map of Guangzhou of 2010 (Guagnzhou Land Resource Administration Bureau, 2010). The Land Use Inventory Map was generated based on field visits and interpretation of aerial photographs. A total of 600 pixels were randomly selected from each of the 14 land cover categories as training data. Each pixel in the training dataset was further examined using high resolution images in Google Earth™ and Landsat images to ensure the land cover labels were correctly assigned. After removing pixels that were deemed incorrect, the remaining 5,070 pixels were used as input to a Random Forest classifier (Breiman, 2001; Gislason, Benediktsson, & Sveinsson, 2006; Zhu, Woodcock, Rogan, & Kellndorfer, 2012) (see Table 2 for sample size of each land cover class category).

3. Methods

3.1. Image preprocessing

All images were atmospherically corrected to surface reflectance. The Landsat 5 and 7 images were processed by the Landsat Ecosystem Disturbance Adaptive Processing System (LEDAPS) (Schmidt, Jenkerson, Masek, Vermote, & Gao, 2013) and the Landsat 8 images were processed by the Landsat 8 Surface Reflectance (L8SR) system (Landsat 8 Product Guide). There are two main differences between the two processing systems. First, LEDAPS is based on the Second Simulation of a Satellite Signal in the Solar Spectrum (6S) radiative transfer model (Masek et al., 2006), whereas the L8SR uses an internal algorithm (Landsat 8 Product Guide). Second, the data sources for atmospheric composition (i.e. pressure, water vapor, air temperature, ozone, and aerosol optical thickness) are different. In LEDAPS, pressure, water vapor, air temperature, and ozone data are derived from the National Centers for Environmental Prediction (NCEP) Grid and the aerosol optical thickness is derived directly from the Landsat imagery. Conversely, the atmospheric information in the L8SR system is mainly derived from MODIS products. As previously reported in other studies it is possible that the differences in the methodology of atmospheric correction

may contribute to inconsistency in surface reflectance (Schroeder, Cohen, Song, Canty, & Yang, 2006). The degree to which this impacts the consistency of Landsat 8 and previous Landsat sensors is discussed in more detail in Section 4.2.

Pixels with clouds, cloud shadows, and snow were removed based upon a two-step method. The first step involves use of the Fmask algorithm to identify clouds and their shadows in a single Landsat image (Zhu, Wang, & Woodcock, 2015; Zhu & Woodcock, 2012). The second step involves use of the Tmask algorithm to further refine the dataset

based on the use of multitemporal information (Zhu & Woodcock, 2014b).

3.2. The CCDC algorithm

The CCDC algorithm makes use of all available Landsat data to estimate time series models and uses the models to predict future observations (Zhu & Woodcock, 2014a; Zhu, Woodcock, Holden, & Yang, 2015). If the values of future observations are outside of the predicted range, a
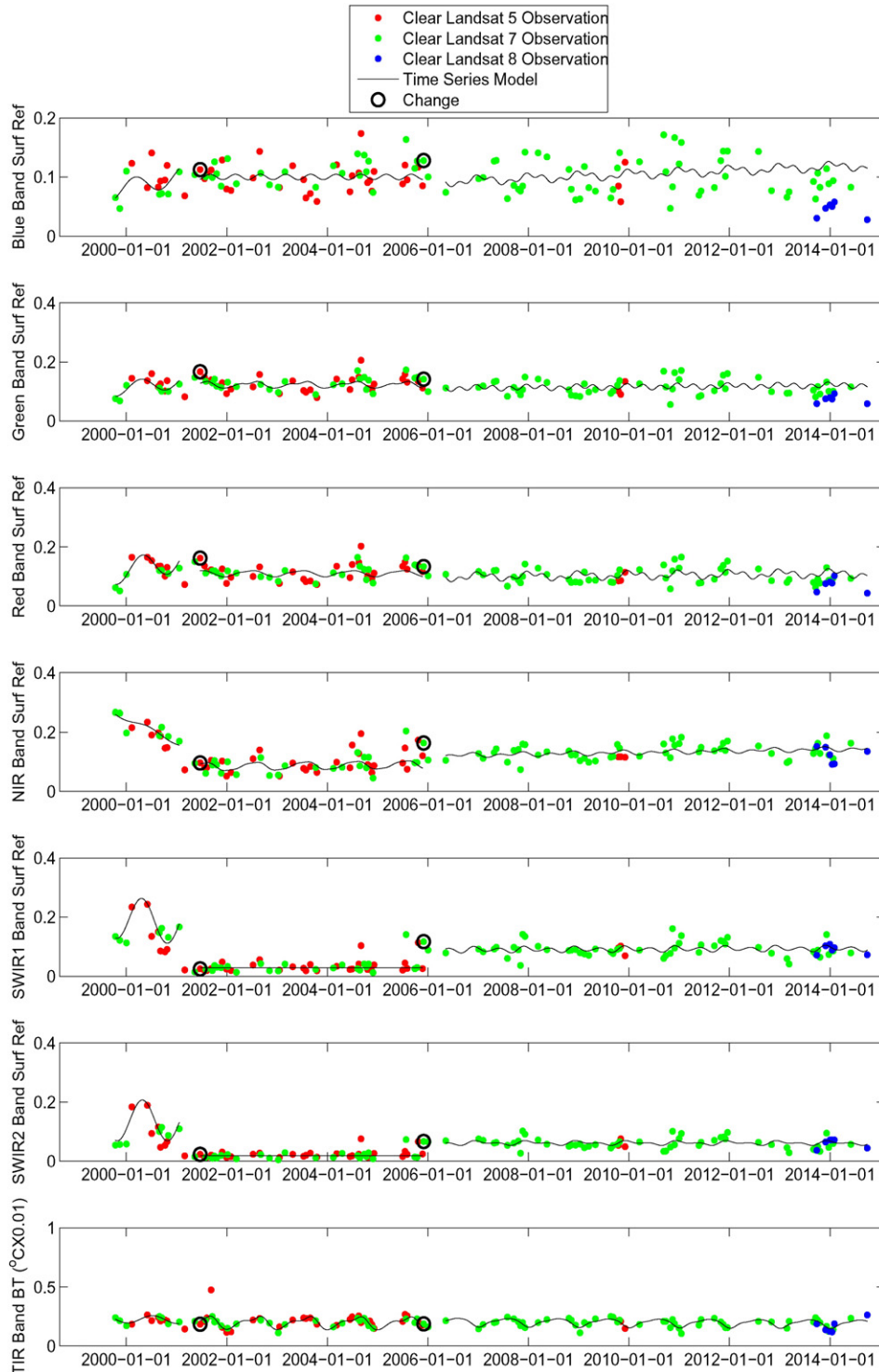

Fig. 2. Illustration of the CCDC algorithm. Landsat 5, 7, and 8 observations are designated by red, green, and blue dots, respectively. Abrupt changes are identified by black circles. Time series models are in black curves. NIR = near-infrared; SWIR1 = shortwave-infrared 1; SWIR2 = shortwave-infrared 2.
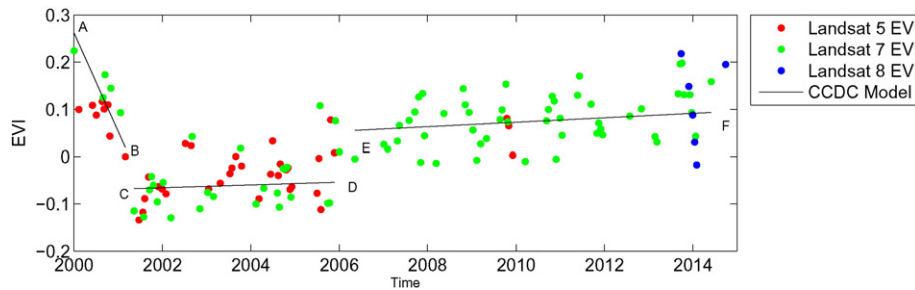
Fig. 3. EVI change estimated by the CCDC method. Red, green, and blue dots are EVI values for Landsat 5, 7, and 8 observations, respectively. The three segments (AB, CD, and EF) are the overall EVI values estimated by the CCDC method. EVI = Enhanced Vegetation Index; CCDC = Continuous Change Detection and Classification.

break is defined in the time series, and new time series models will be estimated once there are enough observations available. As the algorithm combines several spectral bands to define a break, it has the potential of detecting many kinds of land cover change. The time series models are composed of harmonic models (Davis, 1986; Rayner, 1971) that capture the seasonality of the time series, and a slope component that is used for estimating trends. The breaks found in the time series provide information about abrupt changes, such as those caused by land cover changes. By counting how many breaks each pixel has, we are able to generate maps of the total number of changes. On the other hand, by recording when the break is detected, we are able to provide maps of the time of the most recent change.

Instead of classifying the original Landsat images, the coefficients defining the time series models and the Root Mean Square Errors (RMSE) calculated during model estimation are used as the inputs for land cover classification. The Random Forest classifier was applied to each time series interval to provide land cover information at any given time covered by the time series model. Fig. 2 demonstrates how the CCDC algorithm works for a pixel that has undergone multiple land cover changes in Guangzhou. The identified changes are designated by black circles. For this particular pixel, and for each spectral band, there are three models estimated and two breaks detected.

3.3. Analysis of Landsat 8 consistency with prior Landsats

After the time series models are estimated and changes are identified, we can predict the surface reflectance for all Landsat optical bands (Zhu, Woodcock, Holden, & Yang, 2015). Based on the accuracy assessment in Zhu et al. (2015), the difference between the predicted values and the actual observations is similar in magnitude to the noise level (~2 DNs) in Landsat images (Masek, Honzak, Goward, Liu, & Pak, 2001). As CCDC is capable of predicting all 6 optical bands, we can also predict any VIs that can be calculated based on the predicted optical bands. Moreover, since the CCDC algorithm models both seasonal differences and abrupt land cover changes, Landsat 8 observations can be predicted based on historical Landsat 5 and 7 data without being influenced by these factors.

Before predicting Landsat 8 observations, we first analyzed the prediction accuracy of the CCDC algorithm for the study area. Considering that Landsat 5 and 7 data are well calibrated with each other, it is assumed that the difference between predicted and observed Landsat 5 and 7 data would be close to zero if the prediction is accurate. Therefore, we predicted the surface reflectance in 6 optical bands and two VIs for all clear Landsat 5 and 7 observations. Note that the predicted VIs were not directly predicted by model estimation of the observed VIs, but they were calculated based on model estimation of three optical bands (see Eq. (2a, 2b) for details). By comparing model predictions and actual observations of Landsat 5 and 7 data, we calculated the mean differences for all 6 optical bands and two VIs. Later, we tested the consistency of Landsat 8 data by comparing clear Landsat 8 observations with predicted Landsat 8 values based on the time series model estimated by data from Landsat 5 and 7. Because the predictions are more accurate if more observations are available, we only used pixels that had not changed since 2000 for the comparison. Changes in atmospheric conditions could also influence the analysis, therefore, if the difference between predictions and observations was large (more than 0.1 in surface reflectance, or more than 1 in VIs), the observation was excluded from the analysis.

3.4. Trend analysis

Change in greenness can come from three distinct sources: seasonal change, gradual change and abrupt change (Verbesselt et al., 2010; Zhu & Woodcock, 2014a). Seasonal change, mostly driven by vegetation phenology, has a cyclic pattern that is often treated as a source of noise in analysis of greenness trends. Gradual change, caused by vegetation growth, climate change, land degradation, extended drought, pests as well as other factors, changes greenness slowly over long time periods (5 + years), whereas abrupt change, generally induced by land cover change, can have a large impact on greenness within a short time period (1~2 years). If there is no land cover change, a simple method like SLT works well, as only gradual change will contribute to the greenness trends. However, for places experiencing land cover change, the abrupt change can skew the analysis of greenness trends (Cohen, Yang, & Kennedy, 2010; Kennedy, Yang, & Cohen, 2010). Fig. 3 illustrates
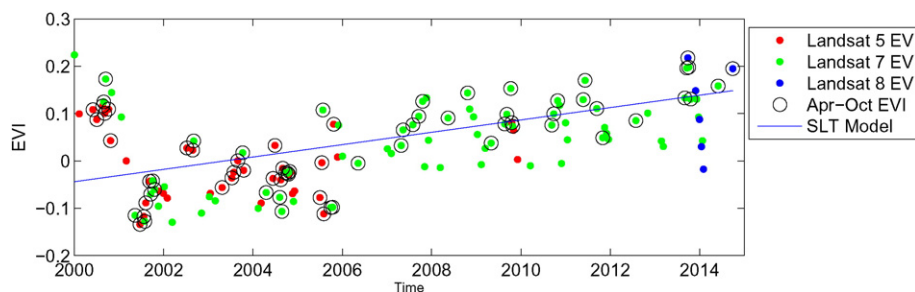

Fig. 4. EVI change estimated by the SLT method for the same pixel shown in Figs. 2 and 3 based on all available growing season (April–October) Landsats 5, 7, and 8 observations. Red, green, and blue dots are EVI values for Landsats 5, 7, and 8 observations, respectively. The blue line is the trend estimated by the SLT method. EVI = Enhanced Vegetation Index; SLT = Simple Linear Trend.
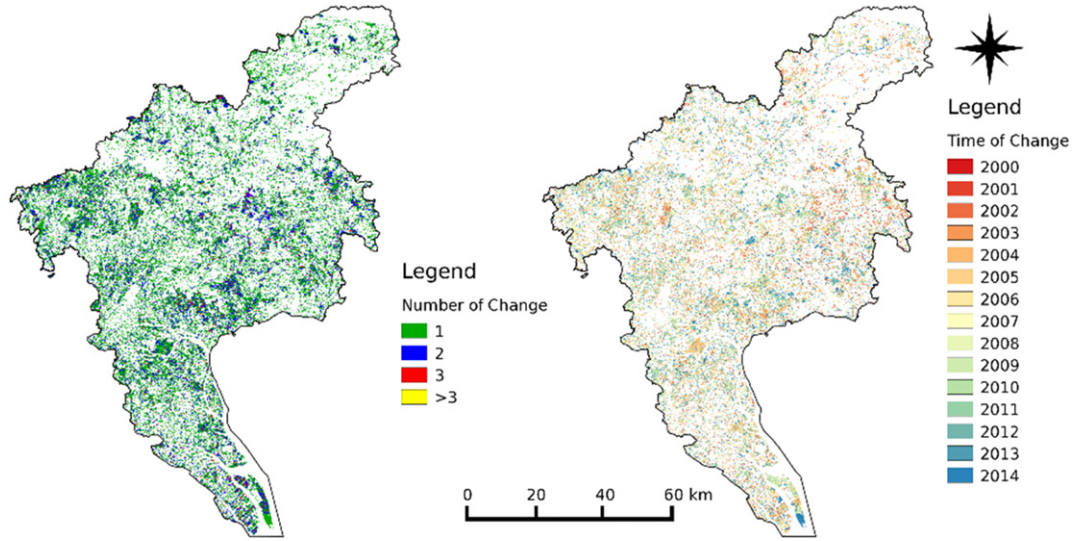
Fig. 5. CCDC 2000–2014 change maps. The map on the left shows the number of changes from 2000 to 2014. The map on the right shows the year of the most recent change.

how the abrupt and gradual changes in greenness (EVI) are calculated based on the CCDC results. The pixel has changed twice since 2000. For each spectral band, three time series models were estimated and the start and end time of each model were also recorded. Therefore, we were able to estimate the overall value for each spectral band for each pixel at the start and end of each time series model (Eq. (1a, 1b)). These values can be used to estimate the overall VI value at the start and end of each segment (Eq. (2)). By assuming that the computed VIs in each time series model would only change linearly, we generate the predicted overall VI segments by linking VI_{start} and VI_{end} (Fig. 3). The accumulated gradual change in each pixel is the sum of the differences in VI at the end VI ($VI_{end,j}$) and the start ($VI_{start,j}$) of all segments (Eq. (3)), and the accumulated abrupt change is the sum of the differences in VI at the start of the next segment ($VI_{start,j+1}$) and the end of the current segment ($VI_{end,j}$) (Eq. (4)). The total CCDC-based estimate of change in greenness is the sum of the accumulated gradual changes and the accumulated abrupt changes (Eq. 5).

$$\rho_{start,i,j} = a_{0,i,j} + t_{start,i,j} \times c_{1,i,j} \tag{1a}$$

$$\rho_{end,i,j} = a_{0,i,j} + t_{end,i,j} \times c_{1,i,j} \tag{1b}$$

Where,

$a_{0,i,j}$: Coefficient for overall value for the ith band and the jth time series model;

$c_{1,i,j}$: Coefficient for inter-annual change (slope) for the ith band and the jth time series model;

i: The ith band;

j: The jth time series model;

$t_{start,i,j}$: Start (Julian date) of the ith band and the jth time series model;

$t_{end,i,j}$: End (Julian date) of the ith band and the jth time series model;

$\rho_{start,i,j}$: Overall value at the start of the ith band and the jth time series model;

$\rho_{end,i,j}$: Overall value at the end of the ith band and the jth time series model.

$$VI_{start,j} = \frac{\rho_{start,NIR,j} - \rho_{start,Red,j}}{\rho_{start,NIR,j} + \rho_{start,Red,j}} \text{ (NDVI) or}$$
$$2.5 \times \frac{\rho_{start,NIR,j} - \rho_{start,Red,j}}{\rho_{start,NIR,j} + 6 \times \rho_{start,Red,j} - 7.5 \times \rho_{start,Blue,j} + 1} \text{ (EVI)} \tag{2a}$$
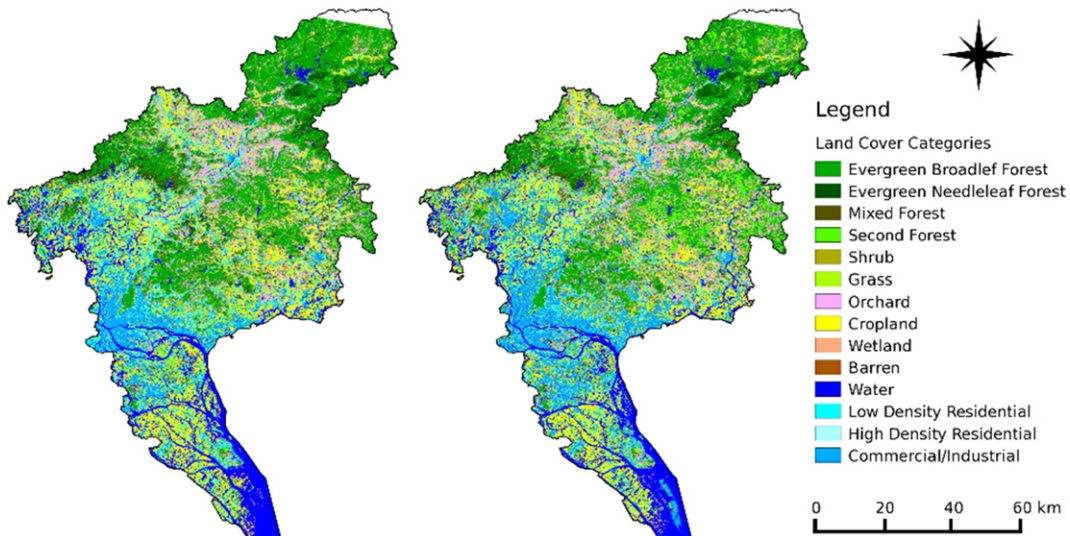

Fig. 6. Land cover maps for 2000 (left) and 2014 (right).

Table 3
Accuracy assessment and area estimate for CCDC land cover and land cover change maps from 2000 to 2014.

	Forest	Urban	Agriculture	Herb	Water	Forest management	Forest loss	Forest gain	Herbaceous gain	Agriculture gain	Water gain	Urban gain
Accuracy measures												
Prod. acc.	90.31%	92.92%	87.39%	60.07%	97.85%	87.53%	85.19%	67.88%	78.30%	80.06%	82.76%	82.25%
User acc.	91.97%	88.32%	92.00%	61.62%	93.33%	74.67%	87.76%	75.51%	73.33%	68.00%	70.00%	97.30%
Overall acc	87.05%											
Stratified estimators of area ± CI [% of total map area]												
Area	22.34%	17.08%	19.61%	5.92%	10.63%	4.31%	3.40%	2.39%	3.62%	2.06%	1.37%	7.30%
95% CI	1.09%	1.00%	1.06%	1.03%	0.69%	0.64%	0.49%	0.50%	0.59%	0.44%	0.38%	0.61%

$$VI_{end,j} = \frac{\rho_{end,NIR,j} - \rho_{end,Red,j}}{\rho_{end,NIR,j} + \rho_{end,Red,j}} \text{ (NDVI) or}$$

$$2.5 \times \frac{\rho_{end,NIR,j} - \rho_{end,Red,j}}{\rho_{end,NIR,j} + 6 \times \rho_{end,Red,j} - 7.5 \times \rho_{end,Blue,j} + 1} \text{ (EVI)} \quad (2b)$$

Where,

$VI_{start,j}$: Estimated overall VI value at the start of *j*th time series model;

$VI_{end,j}$: Estimated overall VI value at the end of *j*th time series model.

$$Gradual = \sum_{j=1}^{K} (VI_{end,j} - VI_{start,j}) \quad (3)$$

K: Total number of time series models estimated for a pixel;
Gradual: Accumulated gradual greenness change based on the CCDC method.

$$Abrupt = \sum_{j=1}^{K-1} (VI_{start,j+1} - VI_{end,j}) \quad (4)$$

Where,

K: Total number of time series models estimated for a pixel;
Abrupt: Accumulated abrupt greenness change based on the CCDC method.

$$Total(CCDC) = Gradual + Abrupt \quad (5)$$

Where, *Total(CCDC)*: Accumulated total greenness change based on the CCDC method.

Fig. 3 illustrates how change in EVI was estimated using the breaks found by CCDC for the same pixel shown in Fig. 2. The red points are the EVI values for all available clear Landsat 5 observations; the green points are Landsat 7 observations; and the blue points are Landsat 8 observations. Points A, C, and E are the EVI values at the start of each time series segment, and points B, D, and F are the corresponding EVI values at the end of segments. In this case, it is possible to calculate the gradual change values: BA (-0.2430), DC (0.0133), and FE (0.0379). We could also calculate the magnitude of the two abrupt change values: CB (-0.0101) and ED (0.0555). By summing these differences, the total EVI change from 2000 to 2014 (FEDCBA) is estimated as -0.1464.

The CCDC greenness change estimates were compared with the widely used SLT method, which was applied to all pixels acquired during the growing season (April-October). The SLT model contains a slope coefficient (Eq. (6)) that provides the greenness trend information. By multiplying the slope coefficient by the total time, the magnitude of total greening change can be calculated (Eq. (7)).

$$VI_t = \alpha + \beta \times t \quad (6)$$

Where,
α: Constant;
β: Slope;
t: Time (Julian date) of the observation;
VI_t: Model estimated VI value for a pixel at time t.

$$Total(SLT) = \beta \times t_{total} \quad (7)$$

Where,

t_{total}: Total time of the time series data;
Total(SLT): Accumulated total greenness change based on the SLT method.

Fig. 4 illustrates the SLT method for the same time series shown in Fig. 2 and 3. The growing season observations are the black circles and the estimated SLT model is the blue line. In this case, the SLT method yielded a very different answer than the CCDC method; the SLT generated a positive trend of greenness (total EVI increased by 0.1926 since 2000), whereas the CCDC answer was negative (-0.1464). While the SLT method was able to capture the growing trend after the first disturbance in 2001, EVI changes that occurred before 2001 were not represented. Moreover, the estimated slope can also be influenced by the procedure of selecting the growing season observations. Although Forkel et al., 2013 found good results using annual aggregated NDVI time series derived from AVHRR data, this may not work well for Landsat time series datasets, which have much lower temporal frequency.

3.5. Accuracy assessment and area estimate

Areas of land cover and land change obtained as sums of map units assigned to relevant map classes – referred to as "pixel counting", are inherently biased because of classification errors. Furthermore, while an error matrix and accuracy measures can provide precision information, they do not directly provide information on the uncertainty of areas (Penman et al., 2014). This holds true regardless of the map that was produced. For these reasons, a sample of reference observations of land cover and land change was collected for construction of unbiased area estimators and for estimating uncertainty compliant with good

Table 4
Mean differences between observed and predicted Landsats 5–7 and Landsat 8 optical bands and VIs.

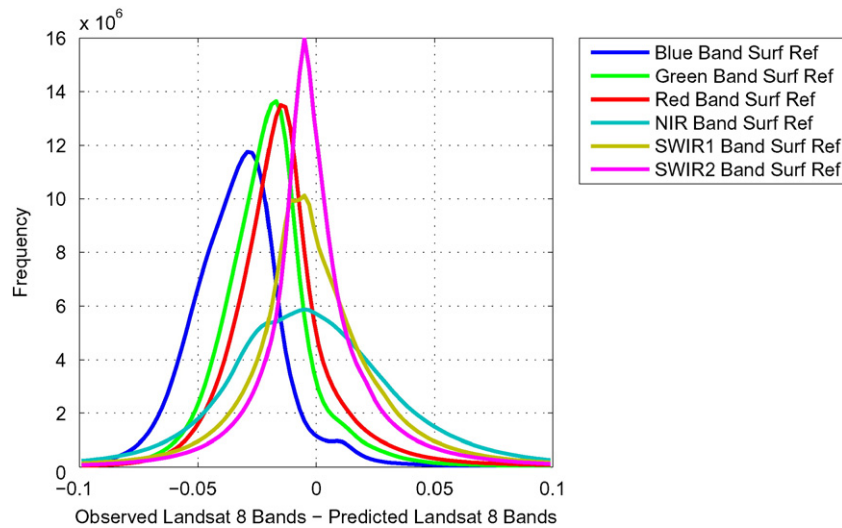| Spectral bands or VIs	Blue	Green	Red	NIR	SWIR1	SWIR2	NDVI	EVI
Mean difference for Landsats 5–7	0.0012	0.0011	0.0010	-0.0003	-0.0010	-0.0013	-0.0046	0.0010
Mean difference for Landsat 8	-0.0332	-0.0203	-0.0147	-0.0025	-0.0015	-0.0015	0.0424	-0.0193

Fig. 7. Histogram of the differences between predicted and observed Landsat 8 six optical bands. NIR = near-infrared; SWIR1 = shortwave-infrared 2; TIR = thermal infrared.

practice guidance (Olofsson et al., 2014). The sample was stratified by a map of 12 classes; 5 stable classes: *forest* (evergreen broadleaf, evergreen needleleaf, mixed, and secondary), *urban*, *agriculture* (farmland and orchards), *herbaceous* (grasslands and shrublands) and *water/wetland*; and 7 change classes: *managed forest*, *forest loss*, and *gains in forest*, *herbaceous*, *agriculture*, *water* and *urban*. A sample of 1245 sample units (pixels) was selected after applying Eq. 5.25 in Cochran (1977) to determine the sample size.

The sample was manually interpreted by three analysts using time series of Landsat data together with GoogleEarth™ imagery and aerial photographs. The composition of land covers in each sample unit and the interpreter's confidence in the provided reference label (low, moderate and high) were recorded. To determine final reference labels, units with larger area proportions and higher confidence were selected. Areas were estimated from the sample by stratified estimation (Cochran, 1977; Olofsson, Foody, Stehman, & Woodcock, 2013) and confidence intervals were constructed for area estimates. Producer's and user's accuracies of map categories and overall accuracy of the map were computed in addition to area estimates.

4. Results and discussions

4.1. Change detection and classification maps

Fig. 5 shows the change maps generated for Guangzhou between 2000 and 2014. The map on the left shows the total number of abrupt changes detected while the map on the right shows the year of the most recent change. A remarkably large proportion of the study area has changed (34%), and most of them (71%) have changed only once. Most of the changes occurred in two time periods, 2003–2004 (orange) and 2012–2013 (blue). Fig. 6 shows the land cover maps for Guangzhou in 2000 and 2014. The three urban classes (*low density residential*, *high density residential*, and *commercial/industrial*) have expanded substantially in the last 15 years. The three forest classes (*evergreen broadleaf forest*, *needleleaf forest*, and *mixed forest*) have been shrinking and are mainly being replaced by *secondary forest*. Large areas of *commercial/industrial* in the 2014 map were *water* in 2000 (in the southeastern part of Guangzhou).

As shown in Table 3, the stable classes were mapped with higher accuracy except for the stable herbaceous class which was aggregated from the *grass* and *shrubland* classes. All area estimates were significant with no margins of errors larger than 28%. Urban areas increased by 7.3 ± 0.6% of the total study area , and the area forest loss (3.4 ± 0.5%) was

slightly larger than the area of forest gain (2.4 ± 0.5%), indicating that the area experienced a net loss of forest from 2000 to 2014.

4.2. Consistency of data from Landsat 8 with Landsat 5 and 7

While the mean differences between predicted and observed data from Landsat 5 and 7 were close to zero, the differences between predicted and actual Landsat 8 data were considerably larger (Table 4). The observed surface reflectance data from Landsat 8 are lower than the predicted values for all 6 optical bands, but the bias in the longer wavelength bands is much less than in the visible bands. The blue band surface reflectance from Landsat 8 is 0.0332 lower than the predicted values, which is quite high relative to the magnitude of blue band surface reflectance. For the VIs, the observed Landsat 8 NDVI value is 0.0424 higher than the predicted values, while the observed EVI value is 0.0193 lower than the predicted values. Fig. 7 illustrates the histogram of the difference between the observed and the predicted Landsat 8 values. It is apparent that all the visible bands are negatively biased in Landsat 8 images. The blue band in Landsat 8 shows the largest bias, followed by the green and red bands, while the NIR, SWIR1, and SWIR2 bands are less biased. Fig. 8 illustrates the difference between
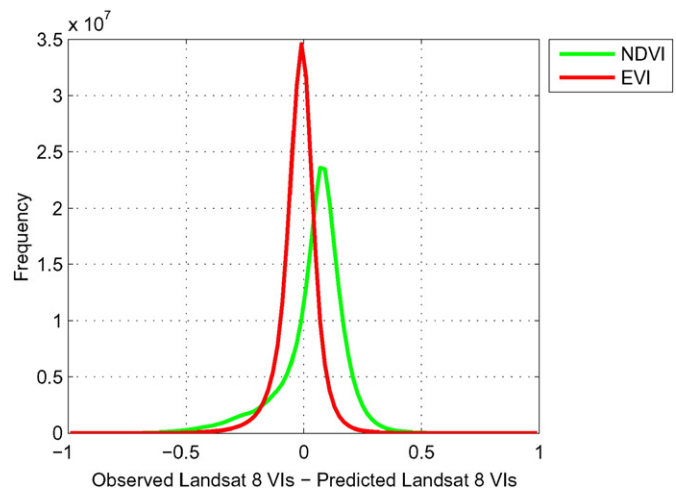

Fig. 8. Histogram of the differences between predicted and observed Landsat 8 VIs. NDVI = Normalized Difference Vegetation Index; EVI = Enhanced Vegetation Index.

predicted Landsat 8 VIs and the observed Landsat 8 VIs. The observed Landsat 8 NDVI values are much higher than the predicted values, while the EVI values are less biased.

We believe that the differences in the visible bands are related to the different atmospheric correction methods used. Compared to the NIR bands, the visible bands of Landsat 8 are more spectrally similar to previous sensors; however, atmospheric correction has larger impacts on the resulting surface reflectance values for the visible bands. The large positive bias in Landsat 8 NDVI values is caused by the negative bias in the red band which makes the denominator smaller and the numerator larger (see Eq. (2) for details). The EVI values are less biased than the NDVI values as the biases of the blue band and the red band cancel each other during the EVI calculation. Although the numerator is larger because of lower red band surface reflectance, the denominator is also larger as the combined effects of 6 times the red band minus 7.5 times blue band (see Eq. (2) for details). Because the Landsat 8 EVI values are less biased than the NDVI values, EVI was used as the indicator of greenness. In the future, to make Landsat 8 data more consistent with data from previous Landsat sensors, using the same atmospheric correction method (including the same atmospheric composition data) for all Landsat data might help alleviate the bias we detected. Note that the current Landsat 8 surface reflectance product is only provisional, and that the U.S. Geological Survey is currently evaluating its surface reflectance correction procedures for Landsat with the hope of improving consistency across time and sensors.

4.3. Changes in greenness estimated by SLT and CCDC

After applying the CCDC and SLT methods for all pixels in the study area, total EVI change maps from 2000 to 2014 based on Eqs. 5 and 7 were produced (Fig. 9). The map on the left in Fig. 9 is the total EVI change derived from the SLT method, and the map on the right is the total EVI change derived from CCDC. The different colors represent change in EVI values over the past 15 years, where the stronger green hues indicate larger increases in EVI, whereas the stronger red hues reflect the greater decreases in EVI. Generally the greenness change patterns between the two methods are quite similar but the SLT greenness trends show much larger change magnitudes in both directions than respective CCDC trends. Fig. 10 is the scatter plot of total EVI change from the CCDC method versus the total EVI change from the SLT method. The colors indicate the density of the points within each grid. Most of the EVI changes from the two methods are positive
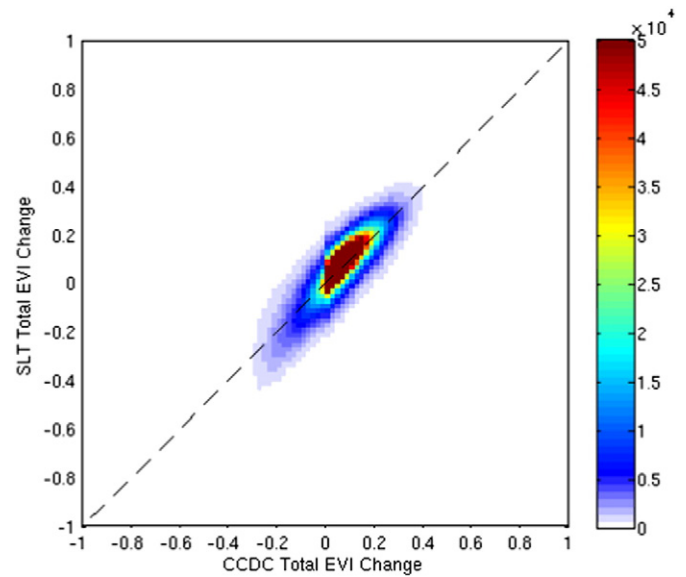

Fig. 10. Scatter plot of CCDC total EVI change versus SLT total EVI change from 2000 to 2014. EVI = Enhanced Vegetation Index; SLT = Simple Linear Trend; CCDC = Continuous Change Detection and Classification. The colors indicate the density of the points within each grid.

(dark red), and the two methods are quite similar. The major difference is that for pixels with positive EVI change, the total greenness change from the SLT method was higher than the CCDC method, while for pixels with negative EVI change, the total greenness change from the SLT method was lower than the CCDC method. Fig. 11 shows the histogram of the total EVI changes from 2000 to 2014 derived from the SLT method (red curve) and the CCDC method (green curve) based on a total of 8.14 million pixels. It is clear that both methods show a greening trend, but that the SLT greenness estimates were higher. The mean total EVI change based on the SLT method was 0.0648, with a 95% confidence interval between 0.0647 and 0.0649. The mean total EVI change based on the CCDC method was 0.0567 and the 95% confidence interval was between 0.0566 and 0.0567. A paired t-test shows that the means of the two distributions were statistically different ($p < 0.01$). Overall, the estimated greenness trends from the SLT method were 14.3% higher than the estimate from the CCDC method.
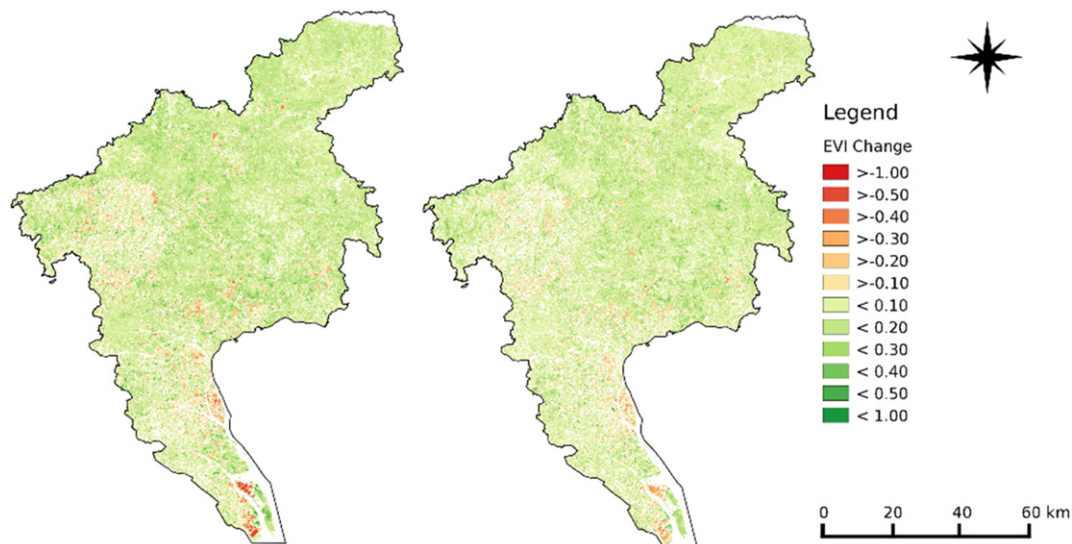

Fig. 9. Total EVI change maps derived by the SLT method (left) and the CCDC method (right) from 2000 to 2014. The colors represent the magnitude of EVI changes. The stronger in red hue, the more decreases in EVI, and the stronger in green hue, the more increases in EVI. EVI = Enhanced Vegetation Index; SLT = Simple Linear Trend; CCDC = Continuous Change Detection and Classification.
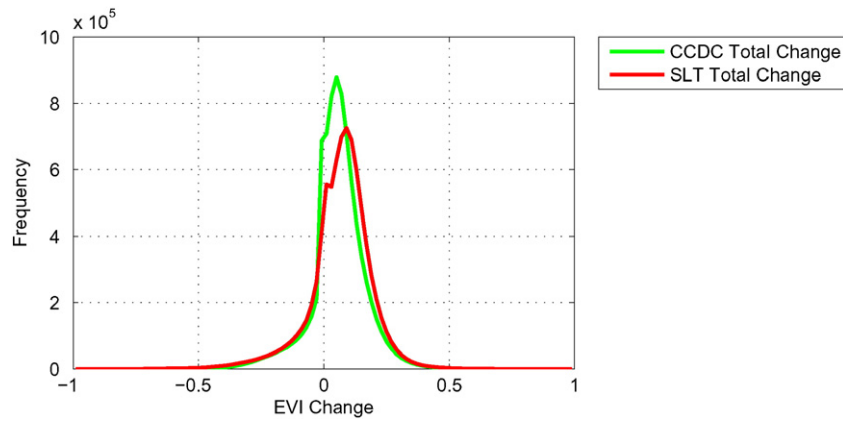
Fig. 11. Histogram of CCDC total EVI change versus SLT total EVI change from 2000 to 2014. EVI = Enhanced Vegetation Index; SLT = Simple Linear Trend; CCDC = Continuous Change Detection and Classification.

As the CCDC algorithm can separate changes in EVI into gradual and abrupt processes, we mapped these forms of change separately from 2000 to 2014 (Fig. 12). For gradual EVI change, except for some of the southeastern areas, most of Guangzhou showed large increases in EVI (green color), even for some highly developed areas. The pixels with abrupt EVI changes showed primarily negative trends, especially for the highly developed areas. It is quite interesting to note that not all land cover changes result in decreased greenness. For the northeastern mountainous areas, some of the land cover changes showed an increase EVI following abrupt changes. Fig. 13 shows a histogram of the gradual and abrupt EVI changes based on the CCDC method. As expected, the abrupt changes tended to be higher in magnitude than the gradual changes. Also, it is interesting to note that the gradual changes tended to be associated with increases in EVI (larger tail on the right), and the abrupt changes generally were associated with decreases in EVI (larger tail on the left). The gradual change histogram (green curve) was based on statistics from 8.16 million pixels, with a mean gradual EVI change of 0.0659, and a 95% confidence interval between 0.0659 and 0.0660. The abrupt change histogram (red curve) was based on all changed pixels (a total of 2.74 million pixels), with a mean abrupt EVI change of −0.0276 and, a 95% confidence interval between −0.0278 and −0.0274. Generally, the abrupt changes had a negative effect on the total greenness. However, the gradual EVI changes had greater influence on the overall results, due to the larger number of pixels and the relatively large magnitude of the mean EVI change.

By averaging the gradual, abrupt, and total change for each individual year for all pixels in the study area, it was possible to provide annual estimates of the mean EVI change magnitude caused by the different change components as well as the total amount of EVI change estimated from the STL and CCDC methods (Fig. 14). For the SLT method, as the slope of the linear model was a constant, the annual estimates of the mean EVI change were a fixed value, except for 2014, during which we did not have a full year of data. It is obvious that at the scale of individual years, the magnitudes of the CCDC total change estimates were quite different from the SLT estimates, especially for the years when many abrupt changes were identified (2003, 2004, and 2013 for example). The annual mean gradual EVI changes were all positive and the magnitude increased after 2003. Conversely, the mean EVI changes for the abrupt changes were generally negative, and the magnitude was higher in 2003, 2004, 2012, and 2013. These were also the years when most of the land cover change occurred. Fig. 15 shows the accumulated mean EVI change, which is similar to Fig. 14, but the values are cumulative through time. Similarly, the gradual changes showed a positive trend, and the abrupt changes showed a negative trend. Although the differences were relatively small, the SLT method consistently overestimated the magnitude of total EVI change compared to the CCDC method.
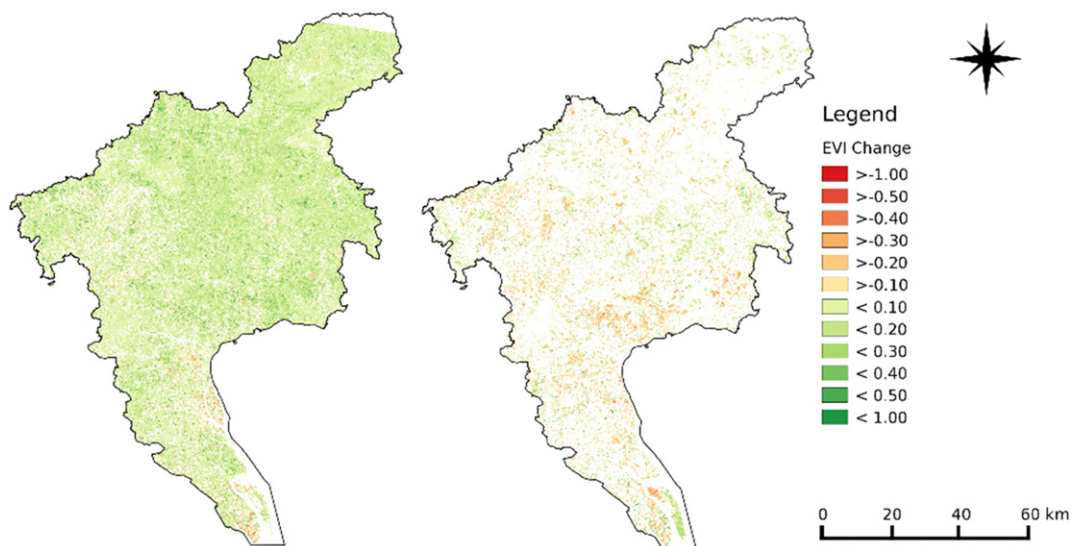

Fig. 12. Gradual (left) and abrupt (right) EVI change maps from 2000 to 2014 derived by the CCDC method. The colors represent the magnitude of EVI changes. The stronger the red hue, the more the decreases in EVI, and the stronger the green hue, the more the increases in EVI. EVI = Enhanced Vegetation Index; CCDC = Continuous Change Detection and Classification.
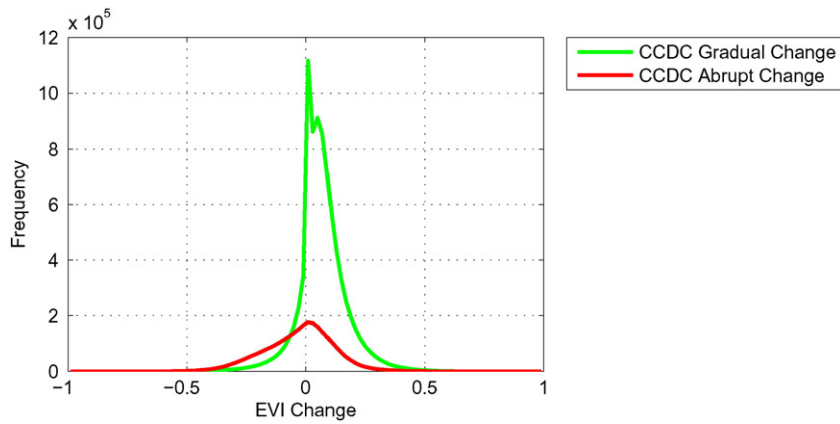
Fig. 13. Histogram of CCDC gradual and abrupt EVI changes occurring from 2000 to 2014. CCDC = Continuous Change Detection and Classification; EVI = Enhanced Vegetation Index.

4.4. Impact of land cover and land cover change on greenness

Using the land cover information for each pixel at any given time, we can quantify the effects of land cover and land cover change on the greenness trends (Figs. 16 and 17). The red bars in Fig. 16 are the average of the gradual changes for all time series models (Eq. (3)) for each land cover category, and the blue bars are the frequency of time series models classified into the same land cover category. Surprisingly, all land cover categories showed positive values in mean gradual EVI change, with *orchard* showing the largest magnitude (~0.15). The mean gradual EVI change for the categories of *water* and *commercial/industrial* were the lowest in magnitude (0.01–0.02). The small positive magnitude in the *water* category might be due to the increased growth of phytoplankton from eutrophication (Li, Huang, Chen, Zhou, & Tan, 2006). Although the mean gradual EVI change in evergreen broadleaf forest was modest (~0.05), because of the large extent of the class, it was one of the main contributors to the overall increase of EVI in terms of gradual change. The red bars in Fig. 17 are the mean abrupt change in EVI for each post-disturbance land cover category (Eq. (4)), and the blue bars represent the frequency of each post-disturbance land cover category. In this case, if the pixels changed to vegetated classes, such as *evergreen broadleaf forest*, *evergreen needleleaf forest*, *mixed forest*, *secondary forest*, *croplands*, and *wetlands*, positive mean abrupt EVI changes were observed. On the other hand, if the change was to classes with less vegetation, such as *barren*, *water*, *low density residential*, *high density residential*, and *commercial/industrial*, negative mean abrupt changes were observed. The largest negative change magnitude

was associated with areas changed to *barren* (~0.15). The *commercial/industrial* class was also one of the most important contributors, as many abrupt changes ended up in this class.

The magnitude of the abrupt EVI change is straightforward to explain, as it was directly related to human activities in Guangzhou. For example, due to the recent "11th Five year" (2006–2010) and "12th Five year" (2011–2015) policies, many areas of old industrial buildings were replaced by new areas of "green space", which had a positive greening effect from the abrupt EVI changes. On the other hand, urban expansion, such as the building of the Guangzhou Higher Education Mega Center and New Baiyun Airport, had a major negative effect on EVI. The magnitude of gradual change is more difficult to understand. Piao et al. (2015) suggested that rising atmospheric CO_2 concentration and nitrogen deposition are the most likely causes of the greening trend in China, and the contribution of nitrogen deposition is more clearly seen in southern China. Factors such as the urban heat island effect (Zhou et al., 2004) and rainfall anomalies (Herrmann et al., 2005) may also influence the vegetation growth in the urban areas. Further studies are needed to better understand the major causes of the greening in Guangzhou.

5. Conclusion

The launch of Landsat 8 extended the continuity of Landsat data. However, the differences in radiometry, band wavelengths, and atmospheric correction methods can cause problems when combining data from previous Landsat satellites for time series analysis. The biggest
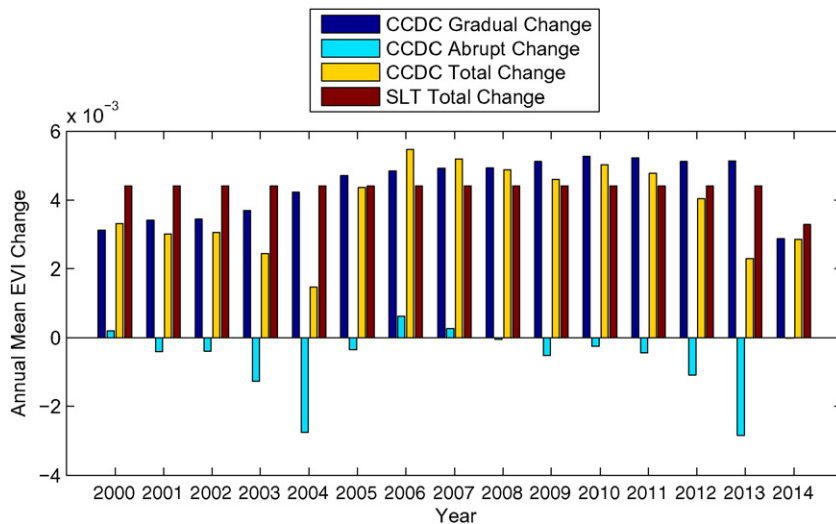

Fig. 14. Annual mean EVI change from the CCDC and SLT methods. For the CCDC method, three annual amounts are provided: CCDC gradual, abrupt, and total change. For the SLT method, only the annual SLT total change can be calculated. EVI = Enhanced Vegetation Index; CCDC = Continuous Change Detection and Classification; SLT = Simple Linear Trend.
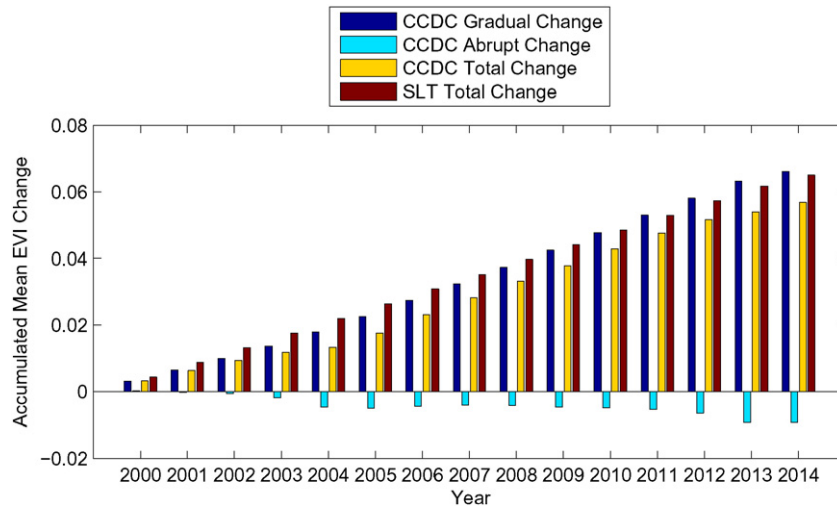
Fig. 15. Accumulated mean EVI change derived from CCDC and SLT methods. For the CCDC method, three accumulated statistical numbers were provided: gradual, abrupt, and total change. For the SLT method, only the accumulated SLT total change can be calculated. EVI = Enhanced Vegetation Index; CCDC = Continuous Change Detection and Classification; SLT = Simple Linear Trend.

differences were in the visible bands, especially the blue band. Landsat 8 NDVI values were positively biased, while Landsat 8 EVI values were less biased compared to NDVI values (slightly negatively biased). We believe the different atmospheric correction methods are the major source of the observed differences.

Land cover change is one factor that can influence the analysis of greenness, and this effect is especially significant for places like Guangzhou that exhibit high rates of change. In comparison with the SLT method, the CCDC-based method presented in this paper provides more detailed and precise estimates of greenness change in areas of land cover change. At the pixel level, the two methods may show different results (e.g. Figs. 3 and 4). The two methods showed large differences in mean annual estimates of EVI change (Fig. 14). The cumulative changes from 2000 to 2014 were less dramatic, but the SLT method still estimated the overall change in greenness to be 14% higher than the CCDC method. Moreover, the CCDC-based method can estimate the effects of gradual change and abrupt separately, provide greenness change for different time intervals, and associate land cover information with greenness change.

Increased EVI was observed in Guangzhou from 2000 to 2014 in spite of the massive urban growth during that time period. Since Landsat 8 EVI was slightly lower than Landsat 5 and Landsat 7 EVI, the magnitude of the actual EVI increase may have been even higher than estimated. Generally, the abrupt change decreased EVI, and the gradual change increased EVI. Because there were many more pixels with gradual change (8.16 million pixels) than the pixels with abrupt change (2.74 million pixels), and because the value of mean gradual EVI change (0.0659) was also larger than the value of the mean abrupt EVI change (-0.0276), the total EVI change in Guangzhou was positive (0.0567).

In conclusion, although data from Landsat 8 are not completely consistent with data from the previous Landsat 5 and 7 satellites, the EVI values are only slightly negatively biased, and therefore we believe that the EVI data can be used for vegetation greenness analysis without further modification. NDVI values appeared to be sufficiently positively
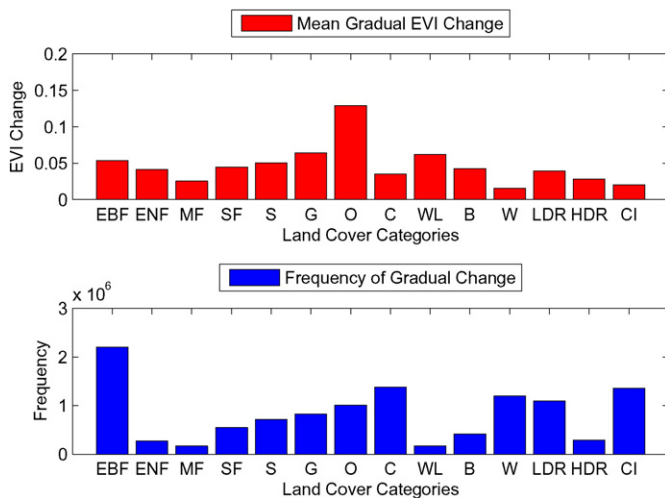

Fig. 16. Magnitude of mean gradual changes for all time series models for different land cover categories (red bars) and the frequency of time series models classified into the same land cover category (blue bars). EBF = *Evergreen Broadleaf Forest*; ENF = *Evergreen Needleleaf Forest*; MF = *Mixed Forest*; SF = *Secondary Forest*; S = *Shrubland*; G = *Grassland*; O = *Orchard*; C = *Croplands*; WL = *Wetland*; B = *Barren*; W = *Water*; LDR = *Low Density Residential*; HDR = *High Density Residential*; CI = *Commercial/Industry*.
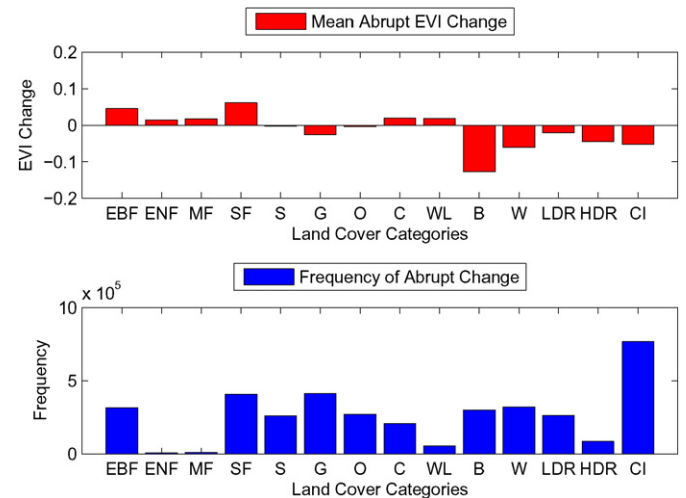
Fig. 17. Magnitude of mean abrupt changes for the land cover categories to which they have changed to (red bars), and the frequency of the land cover categories to which they changed (blue bars). EBF = *Evergreen Broadleaf Forest*; ENF = *Evergreen Needleleaf Forest*; MF = *Mixed Forest*; SF = *Secondary Forest*; S = *Shrubland*; G = *Grassland*; O = *Orchard*; C = *Croplands*; WL = *Wetland*; B = *Barren*; W = *Water*; LDR = *Low Density Residential*; HDR = *High Density Residential*; CI = *Commercial/Industry*.

biased to alter the trend results. Based on this study, we are reluctant to recommend the use of Landsat 8 NDVI data with NDVI data from Landsat 5 and 7 in greenness trend analyses. In addition, it is important to consider land cover change when evaluating trends in greenness, especially for places undergoing surface changes across large areas. For Guangzhou, not considering land cover change for assessing greenness trends can bias the results. Finally, based on all available data collected by Landsat 5, 7, and 8 from 2000 to 2014, Guangzhou has experienced a significant greening. It will be important to perform similar trend studies for other urban areas to determine if the trends in Guangzhou are typical or unique.

Acknowledgements

References

Anderson, G., & Ge, Y. (2004). Do economic reforms accelerate urban growth? The case of China. *Urban Studies, 41*(11), 2197–2210.

Barsi, J. A., Schott, J. R., Palluconi, F. D., Helder, D. L., Hook, S. J., Markham, B. L., ... O'Donnell, E. M. (2003). Landsat TM and ETM+ thermal band calibration. *Canadian Journal of Remote Sensing, 29*(2), 141–153.

Bhatt, U. S., Walker, D. A., Raynolds, M. K., Bieniek, P. A., Epstein, H. E., Comiso, J. C., et al. (2013). Recent declines in warming and vegetation greening trends over pan-Arctic tundra. *Remote Sensing, 5*(9), 4229–4254.

Breiman, L. (2001). Random forests. *Machine Learning, 45*(1), 5–32.

Breshears, D. D., Cobb, N. S., Rich, P. M., Price, K. P., Allen, C. D., Balice, R. G., ... Meyer, C. W. (2005). Regional vegetation die-off in response to global-change-type drought. *Proceedings of the National Academy of Sciences, 102*(42), 15144–15148.

Carlson, T. N., & Ripley, D. A. (1997). On the relation between NDVI, fractional vegetation cover, and leaf area index. *Remote Sensing of Environment, 62*(3), 241–252.

Chander, G., Markham, B. L., & Helder, D. L. (2009). Summary of current radiometric calibration coefficients for Landsat MSS, TM, ETM+, and EO-1 ALI sensors. *Remote Sensing of Environment, 113*(5), 893–903.

Chen, S. S., Chen, L. F., Liu, Q. H., Li, X., & Tan, Q. (2005). Remote sensing and GIS-based integrated analysis of coastal changes and their environmental impacts in Lingding Bay, Pearl River Estuary, South China. *Ocean and Coastal Management, 48*(1), 65–83.

Cochran, W. G. (1977). *Sampling Techniques.* New York, NY: Wiley.

Cohen, W. B., Yang, Z., & Kennedy, R. (2010). Detecting trends in forest disturbance and recovery using yearly Landsat time series: 2. TimeSync—Tools for calibration and validation. *Remote Sensing of Environment, 114*(12), 2911–2924.

Davis, J. C. (1986). *Statistics and Data Analysis in Geology* (2nd ed.). New York, N. Y.: *J. Wiley and Sons*, 646.

Donohue, R. J., McVICAR, T. I. M., & Roderick, M. L. (2009). Climate-related trends in Australian vegetation cover as inferred from satellite observations, 1981–2006. *Global Change Biology, 15*(4), 1025–1039.

Flood, N. (2014). Continuity of reflectance data between Landsat-7 ETM+ and Landsat-8 OLI, for both top-of-atmosphere and surface reflectance: A study in the Australian Landscape. *Remote Sensing, 6*(9), 7952–7970.

Forkel, M., Carvalhais, N., Verbesselt, J., Mahecha, M. D., Neigh, C. S., & Reichstein, M. (2013). Trend change detection in NDVI time series: Effects of inter-annual variability and methodology. *Remote Sensing, 5*(5), 2113–2144.

Fraser, R., Olthof, I., Carrière, M., Deschamps, A., & Pouliot, D. (2012). A method for trend-based change analysis in Arctic tundra using the 25-year Landsat archive. *Polar Record, 48*(01), 83–93.

Friedl, M. A., McIver, D. K., Hodges, J. C., Zhang, X. Y., Muchoney, D., Strahler, A. H., ... Schaaf, C. (2002). Global land cover mapping from MODIS: Algorithms and early results. *Remote Sensing of Environment, 83*(1), 287–302.

Friedl, M. A., Sulla-Menashe, D., Tan, B., Schneider, A., Ramankutty, N., Sibley, A., & Huang, X. (2010). MODIS Collection 5 global land cover: Algorithm refinements and characterization of new datasets. *Remote Sensing of Environment, 114*(1), 168–182.

Fu, Y., Lu, X., Zhou, Y., Zeng, X., & Xia, L. (2013). Assessment impacts of weather and land use/land cover (LULC) change on urban vegetation Net Primary Productivity (NPP): A case study in Guangzhou, China. *Remote Sensing, 5*(8), 4125–4144.

Gislason, P. O., Benediktsson, J. A., & Sveinsson, J. R. (2006). Random forests for land cover classification. *Pattern Recognition Letters, 27*(4), 294–300.

Guagnzhou Land Resource Administration Bureau (2010). *Image Atlas of Guangzhou.* Guangdong: Map Publication.

Guangzhou Statistics Yearbook (2014). http://data.gzstats.gov.cn/gzStat1/chaxun/njsj.jsp (Accessed April 29, 2015)

Guangzhou Yearbook Compilation Committee (2010). Administrative Division and Weather. *In Guangzhou Yearbook (In Chinese)* (pp. 4–5). Guangzhou, China: Guangzhou Yearbook Press Chapter 1.

Hermosilla, T., Wulder, M. A., White, J. C., Coops, N. C., & Hobart, G. W. (2015). An integrated Landsat time series protocol for change detection and generation of annual gap-free surface reflectance composites. *Remote Sensing of Environment, 158*, 220–234.

Herrmann, S. M., Anyamba, A., & Tucker, C. J. (2005). Recent trends in vegetation dynamics in the African Sahel and their relationship to climate. *Global Environmental Change, 15*(4), 394–404.

Huang, C., Goward, S. N., Masek, J. G., Thomas, N., Zhu, Z., & Vogelmann, J. E. (2010). An automated approach for reconstructing recent forest disturbance history using dense Landsat time series stacks. *Remote Sensing of Environment, 114*(1), 183–198.

Huete, A., Didan, K., Miura, T., Rodriguez, E. P., Gao, X., & Ferreira, L. G. (2002). Overview of the radiometric and biophysical performance of the MODIS vegetation indices. *Remote Sensing of Environment, 83*(1), 195–213.

Hun, S. S., & Wong, S. T. (1994). The influence of Chinese reform and pre-reform policies on urban growth in the 1980s. *Urban Geography, 15*(6), 537–564.

Irons, J. R., Dwyer, J. L., & Barsi, J. A. (2012). The next Landsat satellite: The Landsat data continuity mission. *Remote Sensing of Environment, 122*, 11–21.

Jim, C. Y., & Chen, W. Y. (2006). Recreation–amenity use and contingent valuation of urban greenspaces in Guangzhou, China. *Landscape and Urban Planning, 75*, 81–96.

Jim, C. Y., & Chen, W. Y. (2008). Assessing the ecosystem service of air pollutant removal by urban trees in Guangzhou (China). *Journal of Environmental Management, 88*, 665–676.

Jong, R., Verbesselt, J., Schaepman, M. E., & Bruin, S. (2012). Trend changes in global greening and browning: Contribution of short-term trends to longer-term change. *Global Change Biology, 18*(2), 642–655.

Kennedy, R. E., Cohen, W. B., & Schroeder, T. A. (2007). Trajectory-based change detection for automated characterization of forest disturbance dynamics. *Remote Sensing of Environment, 110*(3), 370–386.

Kennedy, R. E., Yang, Z., & Cohen, W. B. (2010). Detecting trends in forest disturbance and recovery using yearly Landsat time series: 1. LandTrendr—Temporal segmentation algorithms. *Remote Sensing of Environment, 114*(12), 2897–2910.

Kovalskyy, V., & Roy, D. P. (2015). A One Year Landsat 8 Conterminous United States Study of Cirrus and Non-Cirrus Clouds. *Remote Sensing, 7*(1), 564–578.

Lehmann, E. A., Wallace, J. F., Caccetta, P. A., Furby, S. L., & Zdunic, K. (2013). Forest cover trends from time series Landsat data for the Australian continent. *International Journal of Applied Earth Observation and Geoinformation, 21*, 453–462.

Li, Y., Huang, L., Chen, J., Zhou, M., & Tan, Y. (2006). Water quality and phytoplankton blooms in the Pearl River estuary. In E. Wolanski (Ed.), *The Environment in Asia Pacific Harbours* (pp. 139–145). Netherlands: Springer.

Li, P., Jiang, L., & Feng, Z. (2014). Cross-Comparison of vegetation indices derived from Landsat-7 enhanced thematic mapper plus (ETM+) and Landsat-8 operational land imager (OLI) sensors. *Remote Sensing, 6*(1), 310–329.

Lin, G. C., & Ho, S. P. (2003). China's land resources and land-use change: Insights from the 1996 land survey. *Land Use Policy, 20*(2), 87–107.

Masek, J. G., Honzak, M., Goward, S. N., Liu, P., & Pak, E. (2001). Landsat-7 ETM+ as an observatory for land cover: Initial radiometric and geometric comparisons with Landsat-5 Thematic Mapper. *Remote Sensing of Environment, 78*(1), 118–130.

Masek, J. G., Huang, C., Wolfe, R., Cohen, W., Hall, F., Kutler, J., & Nelson, P. (2008). North American forest disturbance mapped from a decadal Landsat record. *Remote Sensing of Environment, 112*(6), 2914–2926.

Masek, J. G., Lindsay, F. E., & Goward, S. N. (2000). Dynamics of urban growth in the Washington DC metropolitan area, 1973–1996, from Landsat observations. *International Journal of Remote Sensing, 21*(18), 3473–3486.

Masek, J. G., Vermote, E. F., Saleous, N. E., Wolfe, R., Hall, F. G., & Huemmrich, K. F. (2006). A Landsat surface reflectance dataset for North America, 1990–2000. *Geoscience and Remote Sensing Letters, IEEE, 3*(1), 68–72.

McPherson, G. E., Nowak, D., Heisler, G., Grimmond, S., Souch, C., Grant, R., & Rowntree, R. (1997). Quantifying urban forest structure, function, and value: The Chicago Urban Forest Climate Project. *Urban Ecosystems., 1*, 49–61.

Myneni, R. B., Hall, F. G., Sellers, P. J., & Marshak, A. L. (1995). The interpretation of spectral vegetation indexes. *Geoscience and Remote Sensing, IEEE Transactions on, 33*(2), 481–486.

Myneni, R. B., Keeling, C. D., Tucker, C. J., Asrar, G., & Nemani, R. R. (1997). Increased plant growth in the northern high latitudes from 1981 to 1991. *Nature, 386*(6626), 698–702.

Nowak, D. J., Crane, D. E., & Stevens, J. C. (2006). Air pollution removal by urban trees and shrubs in the United States. *Urban Forestry & Urban Greening, 4*(3), 115–123.

Olofsson, P., & Eklundh, L. (2007). Estimation of absorbed PAR across Scandinavia from satellite measurements. Part II: Modeling and evaluating the fractional absorption. *Remote Sensing of Environment, 110*(2), 240–251.

Olofsson, P., Foody, G. M., Herold, M., Stehman, S. V., Woodcock, C. E., & Wulder, M. A. (2014). Good practices for estimating area and assessing accuracy of land change. *Remote Sensing of Environment, 148*, 42–57.

Olofsson, P., Foody, G. M., Stehman, S. V., & Woodcock, C. E. (2013). Making better use of accuracy data in land change studies: Estimating accuracy and area and quantifying uncertainty using stratified estimation. *Remote Sensing of Environment, 129*, 122–131.

Olofsson, P., Lagergren, F., Lindroth, A., Lindström, J., Klemedtsson, L., Kutsch, W., & Eklundh, L. (2008). Towards operational remote sensing of forest carbon balance across Northern Europe. *Biogeosciences, 5*(3), 817–832.

Olsson, L., Eklundh, L., & Ardö, J. (2005). A recent greening of the Sahel—trends, patterns and potential causes. *Journal of Arid Environments, 63*(3), 556–566.

Penman, J., Baltuck, M., Green, C., Olofsson, P., Raison, J., & Woodcock, C. E. (2014). *Integrating remote-sensing and ground-based observations for estimation of emissions and removals of greenhouse gases in forests: Methods and guidance from the global forest observations initiative* (1st ed.). Geneva, Switzerland: Group on Earth Observation.

Piao, S., Yin, G., Tan, J., Cheng, L., Huang, M., Li, Y., et al. (2015). Detection and attribution of vegetation greening trend in China over the last 30 years. *Global Change Biology, 21*(4), 1601–1609.

Rayner, J. N. (1971). *An Introduction to Spectral Analysis.* London: Pion Ltd, 174.

Roy, D. P., Wulder, M. A., Loveland, T. R., Woodcock, C. E., Allen, R. G., & Anderson, M. C. (2014). Landsat-8: Science and product vision for terrestrial global change research. *Remote Sensing of Environment, 145*, 154–172.

Rozenstein, O., Qin, Z., Derimian, Y., & Karnieli, A. (2014). Derivation of land surface temperature for Landsat-8 TIRS using a split window algorithm. *Sensors, 14*(4), 5768–5780.

Schmidt, G., Jenkerson, C., Masek, J., Vermote, E., & Gao, F. (2013). *Landsat ecosystem disturbance adaptive processing system (LEDAPS) algorithm description* (No. 2013–1057). *US Geological Survey.*

Schroeder, T. A., Cohen, W. B., Song, C., Canty, M. J., & Yang, Z. (2006). Radiometric correction of multi-temporal Landsat data for characterization of early successional forest patterns in western Oregon. *Remote Sensing of Environment, 103*(1), 16–26.

Seto, K. C., & Fragkias, M. (2005). Quantifying spatiotemporal patterns of urban land-use change in four cities of China with time series landscape metrics. *Landscape Ecology, 20*(7), 871–888.

Seto, K. C., Woodcock, C. E., Song, C., Huang, X., Lu, J., & Kaufmann, R. K. (2002). Monitoring land-use change in the Pearl River Delta using Landsat TM. *International Journal of Remote Sensing, 23*(10), 1985–2004.

Sonnenschein, R., Kuemmerle, T., Udelhoven, T., Stellmes, M., & Hostert, P. (2011). Differences in Landsat-based trend analyses in drylands due to the choice of vegetation estimate. *Remote Sensing of Environment, 115*(6), 1408–1420.

Teillet, P. M., Barker, J. L., Markham, B. L., Irish, R. R., Fedosejevs, G., & Storey, J. C. (2001). Radiometric cross-calibration of the Landsat-7 ETM + and Landsat-5 TM sensors based on tandem data sets. *Remote Sensing of Environment, 78*(1), 39–54.

Tucker, C. J. (1979). Red and photographic infrared linear combinations for monitoring vegetation. *Remote Sensing of Environment, 8*, 127–150.

Tucker, C. J., Pinzon, J. E., Brown, M. E., Slayback, D. A., Pak, E. W., Mahoney, R., et al. (2005). An extended AVHRR 8km NDVI dataset compatible with MODIS and SPOT vegetation NDVI data. *International Journal of Remote Sensing, 26*(20), 4485–4498.

Verbesselt, J., Hyndman, R., Newnham, G., & Culvenor, D. (2010). Detecting trend and seasonal changes in satellite image time series. *Remote Sensing of Environment, 114*(1), 106–115.

Vogelmann, J. E., Tolk, B., & Zhu, Z. (2009). Monitoring forest changes in the southwestern United States using multitemporal Landsat data. *Remote Sensing of Environment, 113*(8), 1739–1748.

Vogelmann, J. E., Xian, G., Homer, C., & Tolk, B. (2012). Monitoring gradual ecosystem change using Landsat time series analyses: Case studies in selected forest and rangeland ecosystems. *Remote Sensing of Environment, 122*, 92–105.

Weng, Q., & Yang, S. (2003). An approach to evaluation of sustainability for Guangzhou's urban ecosystem. *The International Journal of Sustainable Development & World Ecology, 10*(1), 69–81.

Wulder, M. A., White, J. C., Goward, S. N., Masek, J. G., Irons, J. R., Herold, M., et al. (2008). Landsat continuity: Issues and opportunities for land cover monitoring. *Remote Sensing of Environment, 112*(3), 955–969.

Yang, X., & Lo, C. P. (2002). Using a time series of satellite imagery to detect land use and land cover changes in the Atlanta, Georgia metropolitan area.*International. Journal of Remote Sensing, 23*(9), 1775–1798.

Yuan, F., Sawaya, K. E., Loeffelholz, B. C., & Bauer, M. E. (2005). Land cover classification and change analysis of the Twin Cities (Minnesota) Metropolitan Area by multitemporal Landsat remote sensing. *Remote Sensing of Environment, 98*(2), 317–328.

Zhou, L., Dickinson, R. E., Tian, Y., Fang, J., Li, Q., Kaufmann, R. K., et al. (2004). Evidence for a significant urbanization effect on climate in China. *Proceedings of the National Academy of Sciences of the United States of America, 101*(26), 9540–9544.

Zhou, L., Tian, Y., Myneni, R. B., Ciais, P., Saatchi, S., Liu, Y. Y., et al. (2014). Widespread decline of Congo rainforest greenness in the past decade. *Nature, 509*(7498), 86–90.

Zhou, L., Tucker, C. J., Kaufmann, R. K., Slayback, D., Shabanov, N. V., & Myneni, R. B. (2001). Variations in northern vegetation activity inferred from satellite data of vegetation index during 1981 to 1999. *Journal of Geophysical Research: Atmospheres (1984–2012), 106*(D17), 20069–20083.

Zhu, Z., & Woodcock, C. E. (2012). Object-based cloud and cloud shadow detection in Landsat imagery. *Remote Sensing of Environment, 118*, 83–94.

Zhu, Z., & Woodcock, C. E. (2014a). Continuous change detection and classification of land cover using all available Landsat data. *Remote Sensing of Environment, 144*, 152–171.

Zhu, Z., & Woodcock, C. E. (2014b). Automated cloud, cloud shadow, and snow detection in multitemporal Landsat data: An algorithm designed specifically for monitoring land cover change. *Remote Sensing of Environment, 152*, 217–234.

Zhu, Z., Woodcock, C. E., Rogan, J., & Kellndorfer, J. (2012). Assessment of spectral, polarimetric, temporal, and spatial dimensions for urban and peri-urban land cover classification using Landsat and SAR data. *Remote Sensing of Environment, 117*, 72–82.

Zhu, Z., Wang, S., & Woodcock, C. E. (2015). Improvement and expansion of the Fmask algorithm: Cloud, cloud shadow, and snow detection for Landsats 4–7, 8, and Sentinel 2 images. *Remote Sensing of Environment, 159*, 269–277.

Zhu, Z., Woodcock, C. E., Holden, C., & Yang, Z. (2015). Generating synthetic Landsat images based on all available Landsat data: Predicting Landsat surface reflectance at any given time. *Remote Sensing of Environment, 162*, 67–83.

Further reading

Zhu, Z., Woodcock, C. E., & Olofsson, P. (2012). Continuous monitoring of forest disturbance using all available Landsat imagery. *Remote Sensing of Environment, 122*, 75–91.